A high-performance organic cathode customized for sulfide-based all-solid-state batteries

Abstract

All-solid-state batteries (ASSBs) have become increasingly attractive recently due to their better safety and prospective long-term stability compared with conventional liquid batteries. However, obtaining a sustainable cathode candidate to match the solid electrolyte with regards to operating potential, chemical compatibility, and mechanical property is still an open challenge. Herein, the chemical incompatibility of quinone-based active materials and sulfide-based electrolyte were unveiled for the first time through a heteroconjugate addition reaction mechanism. To develop a quinone cathode customized for sulfide-based ASSBs, poly-(anthraquinonyl sulfide)-graphene (PAQS-G) nanocomposite was reported. The stable polymer framework of PAQS can protect the quinone redox center by preventing nucleophilic attack from sulfide-based solid electrolytes. The graphene additives can ameliorate redox kinetics and improve active material utilization. The PAQS-G cathode exhibited a specific capacity of ~178 mAh g^{-1} and a high material utilization of ~79%. Excellent cycling stability was achieved with 94 % capacity after 200 cycles in lithium batteries and 95.5 % capacity after 300 cycles in sodium batteries at 0.1C rate, respectively. A promising potential for energy storage applications was demonstrated.

Keywords

Organic cathode; Chemical compatibility; Sulfide-based electrolytes; All-solid-state lithium batteries; All-solid-state sodium batteries

Introduction

The demand for intrinsically safe and long-cycle life Li rechargeable batteries has spurred a strong interest in all-solid-state batteries (ASSBs).[1-4] As leading candidates for ASSB cathodes, transitional metal oxides-based materials ($LiNi_{1-x-y}Mn_xCo_yO_2$, etc.) still face many challenges associated with structural instability during cycling, scarcity of ore resources, environmental impact of toxic mining waste and battery disposal.[5] Moreover, the notorious interface issues raised by irreversible electrolyte oxidation under a high potential and interparticle contact failures during cycling can further impede the commercial deployment of ASSBs.[6-10] As an alternative, organic-based redox-active materials show distinct advantages in material abundance, environmental benignancy, structural diversity, and a well-studied redox mechanism.[11-13] More excitingly, the unique elastic nature of the organic materials also secures an intimate inter-particle contact during cycling.[14] Regarding solid electrolytes, sulfide-based electrolytes are very promising due to their high ionic conductivity (>1 mS cm^{-1} at 25 °C), soft mechanical property, and facile processability.[15-17] For example, researchers from Samsung reported a prototype pouch cell with an impressive lifespan of over 1000 cycles and an energy density of 900 Wh L^{-1} by employing argyrodite sulfide (Li_6PS_5Cl) as an electrolyte.[18] Therefore, developing a reliable organic cathode tailored for sulfide-based ASSBs is of great interest.

Quinones are considered as one of the most promising organic electrode materials so far, due to their high theoretical capacity, fast reaction kinetics, and structural tunability.[19-21] To design a quinone material customized for sulfide-based ASSBs, it is particularly critical for the molecule to be chemically compatible with a sulfide-based electrolyte. Since the PS_4^{3-} thiophosphate unit of the sulfide-based electrolyte can act as a strong nucleophilic reagent, they can react with the strongly electrophilic quinone molecules.[22] Such additions quench the redox centers of the quinone structure, leading to a fast decay of attainable capacity. Moreover, the bulk ionic conductivity of the solid electrolyte can also be adversely affected. On the other hand, the intrinsic insulating nature of most organic compounds can result in a poor electronic percolation network within a cathode and thereby severely hinder the full utilization of active material. Due to the above issues, only four organic cathodes have been demonstrated in sulfide-based ASSBs thus far: carboxylated azo[23], sodium rhodizonate[24], pyrene-

4,5,9,10-tetraone[14, 25, 26], and truxenone-based covalent organic framework[27]. These organic cathodes still suffer from low capacity or synthetic complexity. Therefore, exploiting a practical organic material with high compatibility toward sulfide electrolyte and efficient conductive network for ASSBs is still an open challenge.

Our continuing interests in electrophotocatalysis with a quinone derivative catalyst DDQ (2,3-dichloro-5,6-dicyano-1,4-benzoquinone) and organic battery materials have inspired us to explore quinone-type cathode materials in sulfide-based all-solid-state batteries.[28-31] In this communication, the undesired heteroconjugate reaction between small quinone compounds and sulfide electrolyte was deciphered for the first time. To enhance the adaptability of quinones toward sulfide electrolyte, poly-(anthraquinonyl sulfide)-graphene (PAQS-G) was adopted. The stable anthroquinone-derived polymer framework of PAQS can protect the otherwise reactive sites of the quinone nucleus by precluding them from the nucleophilic attack. On the other hand, the PAQS-G nanocomposite enables an ameliorated electronic percolation network within the cathode, thanks to a graphene additive. PAQS-G|Li_6PS_5Cl|Li cell exhibited a capacity retention of 94 % after 200 cycles and PAQS-G|Na_3PS_4|$Na_{15}Sn_4$ cell shows a retention 95.5 % after 300 cycles. This work highlights the vital role of chemical protection on the chemical compatibility of organic compounds. Microstructural engineering on an electronic percolation network opens another door for achieving high material utilization in organic solid-state batteries.

2. Results and discussion

2.1. Characterization of solid electrolytes and their compatibility with metallic anodes.

Before inspecting quinone cathode materials, an investigation on solid electrolytes and the anode/electrolyte interface was carried out. A sulfide-based Li_6PS_5Cl electrolyte and metallic lithium anode were selected for all-solid-state lithium batteries. Na_3PS_4 electrolyte and $Na_{15}Sn_4$ alloy anode were adopted for all-solid-state sodium batteries. The more stable $Na_{15}Sn_4$ alloy (0.1 V vs. Na^+/Na) was chosen over metallic Na as the anode, because the Na/Na_3PS_4 interface is electrically conductive and a passivation layer can grow rapidly at the interface upon cycling, causing an increase of cell impedance.[32] Both electrolytes were prepared by a mechanochemical approach followed by a short annealing step.[33] XRD patterns and ionic conductivity are shown in Figure 1a-b. The Li_6PS_5Cl phase existed in a well-formed cubic structure with an ionic conductivity of 1.8 mS cm^{-1} while Na_3PS_4 showed a cubic crystal structure with an ionic conductivity of 0.2 mS cm^{-1} at 25 °C. The galvanostatic cycling performance of symmetric cells was carried out next to ascertain the interfacial stability at the anode side. An insulating polyetheretherketone (PEEK) fixture was designed and shown in Figure 1c to control the stack pressure upon cycling. In our case, an optimal pressure of 10 MPa was enough to ensure good interfacial contact but not too high to induce a short circuit. As shown in Figure 1d, after 1000 h of cycling at 0.2 mA cm^{-2}, the Li|Li_6PS_5Cl|Li symmetric cell shows a slowly increased overpotential from 50 mV to 100 mV, indicating a kinetically stable Li/Li_6PS_5Cl interface. As shown in Figure 1e, the cycling of the $Na_{15}Sn_4$|Na_3PS_4|$Na_{15}Sn_4$ symmetric cell exhibits an overpotential of ~400 mV after 1000 h of cycling at 0.1 mA cm^{-2}.

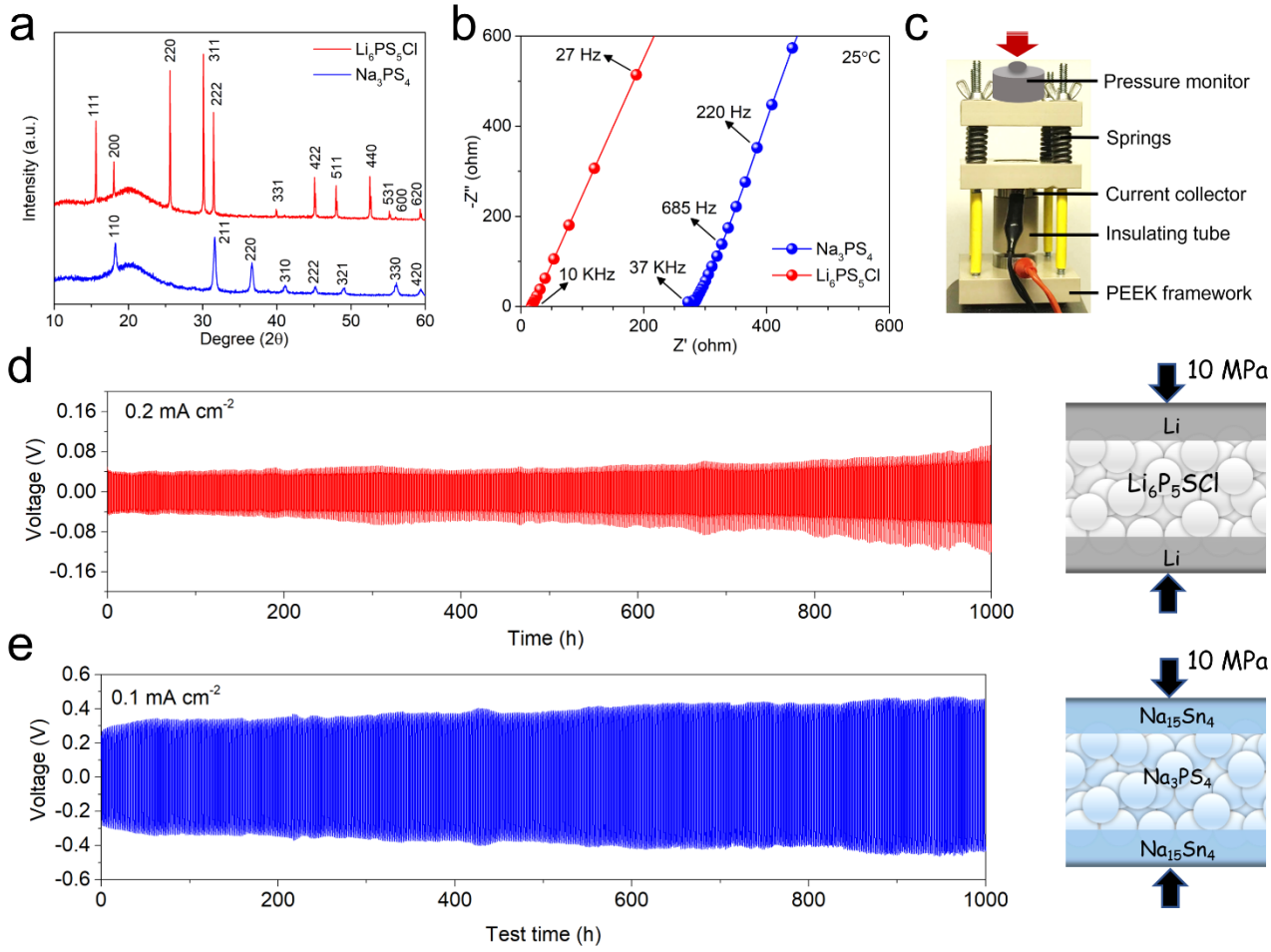

Figure 1. a) XRD pattern and b) ionic conductivity measurement of Li_6PS_5Cl and Na_3PS_4 solid electrolytes at 25°C; c) mechanically constricted design of solid-state cell; cycling performance of d) Li|Li_6PS_5Cl|Li symmetric cell at 0.2 mA cm^{-2} and e) $Na_{14}Sn_5$|Na_3PS_4|$Na_{14}Sn_5$ symmetric cell at 0.1 mA cm^{-2}.

2.2. Mechanism investigation on the compatibility between quinone compounds and sulfide-based electrolyte.

Two classical quinones, p-benzoquinone (BQ) and anthraquinone (AQ), were first explored in the cell configuration of BQ(AQ)|Li_6PS_5Cl|Li. As shown in Figure 2a, the BQ cathode barely exhibits voltage plateau, and the practical capacity is far below its theoretical value (496 mAh g^{-1}). As shown in Figure 2b, the AQ cathode reaches a capacity of ~250 mAh g^{-1} at the initial discharge but quickly fades to ~100 mAh g^{-1} after 16 cycles, equal to 40% of its initial capacity. *In-situ* ^{13}C NMR spectroscopy was employed to study the chemical structure evolution of quinone cathodes. As shown in Figure 2c (up), the chemical shift of pristine BQ is 188 ppm and 137 ppm, assigned to C(1) and C(2) as indicated in BQ's structure. After mixing with carbon-free Li_6PS_5Cl (Figure 2c, down), the chemical shift of pristine BQ disappeared and three new peaks occurred at 150 ppm, 117 ppm, and 17 ppm, respectively. Moreover, as presented in the picture, the white Li_6PS_5Cl pellet rapidly transformed into dark blue once in contact with BQ cathode powder. AQ is a common precursor used in dye industry. Its color can be adjusted with the introduction of electron donor groups onto its structural unit.[34] Figure 2d shows pristine AQ (yellow) and Li_6PS_5Cl (white) and a mixture of both homogenized by hand ground and ball-milling approach. The color of mixtures turned to light green after being hand ground and deep green after energy-intensive ball-milling. As shown in Figure 2e, AQ has converted into other compounds as verified by *in-situ* ^{1}H and ^{13}C NMR spectroscopy. A cyclic voltammetry (CV) experiment was further carried out to investigate the redox reversibility of the AQ cathode reclaimed from the failed solid-state cell. As shown in Figure 2f, the retrieved AQ cathode pellet is immersed in an ether electrolyte, so that the AQ-related products can dissolve while other cathode components (C and Li_6PS_5Cl) remain stable or insoluble.[35] As shown in Figure

2g, the CV profile of the reclaimed AQ cathode becomes severely distorted compared with the pristine AQ, indicating the decomposition of the redox center in the AQ molecule. A possible degradation mechanism is proposed in Figure 2h (left). Small quinone molecules such as BQ can undergo facile nucleophilic addition when exposed to sulfur nucleophiles, such as the Li_6PS_5Cl electrolyte, and form some unidentified products.[22] To prevent the redox centers from being attacked, poly-(anthraquinonyl sulfide) (PAQS) (Figure 2h, right) with a stable polymer framework was adopted, displaying an improved compatibility against sulfide electrolytes via chemoprotection of the quinone group.

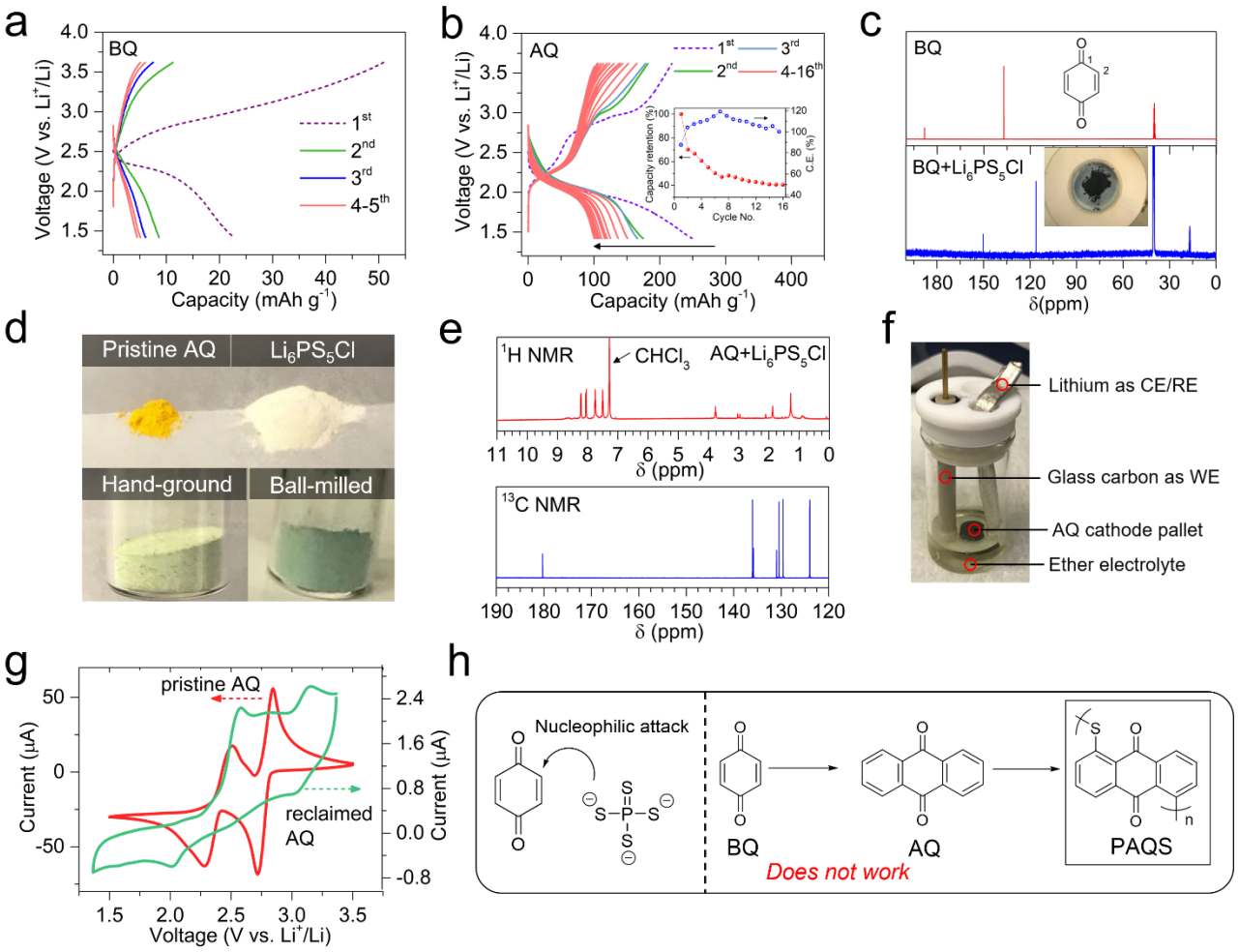

Figure 2. a) Galvanostatic voltage profiles of BQ cathode; b) galvanostatic voltage profiles of AQ cathode, inset is capacity retention and Coulombic efficiency vs. cycle number; c) *in-situ* ^{13}C NMR spectra of pristine BQ and BQ+Li_6PS_5Cl mixture, inset photo demonstrates BQ cathode powder spread on top of Li_6PS_5Cl pellet; d) photos of the pristine AQ, Li_6PS_5Cl powder, and AQ+Li_6PS_5Cl mixture obtained after hand ground and ball milling, respectively; e) *in-situ* ^1H NMR and ^{13}C NMR spectra of AQ+Li_6PS_5Cl mixture; f) a photo of two-electrode CV setup; g) CV profiles of pristine AQ and reclaimed AQ cathode in 1M LiTFSI+DOL/DME electrolyte, the scan rate is 20 mV s^{-1}; h) left: a possible degradation pathway of BQ when exposing to sulfide-based electrolyte, right: structural engineering of BQ to achieve PAQS polymer.

2.3. Material characterization of PAQS-graphene cathode.

To establish an electronic percolation network within the cathode, graphene sheets with extraordinary electronic conductivity were incorporated to form the PAQS-G nanocomposite. Specifically, the PAQS-G nanocomposite was prepared via a one-pot synthesis approach, which facilitated the dispersion and utilization of graphene during the polymerization process of

PAQS.[36] The chemical structure of the PAQS-G nanocomposite was confirmed by FT-IR (Figure S1) and a high thermal stability up to 350°C was verified by a TGA analysis (Figure S2), making it a superb cathode candidate for solid-state batteries at an elevated temperature.[37] As shown in Figure S3, the morphology of the PAQS-G nanocomposite reveals that the graphene sheets were homogeneously embedded in the polymer matrix, capable of providing a fast electron transport by contacting intimately with the polymer. The electronic conductivity was measured to be 0.017 mS cm^{-1} for a pure PAQS compared with 1.18 mS cm^{-1} for the PAQS-G with a graphene content of 20 wt. % (Figure 3a). The conductivity of PAQS-G nanocomposite material is higher than the most common cathode materials (10^{-6} to 10^{-4} S cm^{-1}), so no extra carbon additives is demanded.[38,39] The PAQS-G cathode composite was prepared by ball milling the sulfide electrolyte and the PAQS-G at a weight ratio of 1:1. As shown in Figure 3b and Figure S5, the chemical compatibility of the PAQS-G nanocomposite toward the sulfide electrolyte was validated by an *in-situ* NMR analysis. ^{1}H chemical shift of the PAQS-G+Li_6PS_5Cl composite agreed well with those of the pristine PAQS-G nanocomposite, indicating the redox center of PAQS was completely intact due to the protective effect of the anthroquinone structure. As shown in Figure 3c, top-view SEM image and EDX mapping displayed a homogeneous distribution of cathode components, including particle-like PAQS and Li_6PS_5Cl, as well as wrinkled graphene sheets. As displayed in Figure 3d, the thickness of the electrolyte/cathode layer and cathode layer after cold press is measured to be 621 μm and 78 μm, respectively. The thickness and the density of the Li_6PS_5Cl layer was then calculated to be 543 μm and 1.45 g cm^{-3}, respectively. The EDX mapping of the cross-section view further confirmed the relatively intimate contact between the cathode and the electrolyte layer.

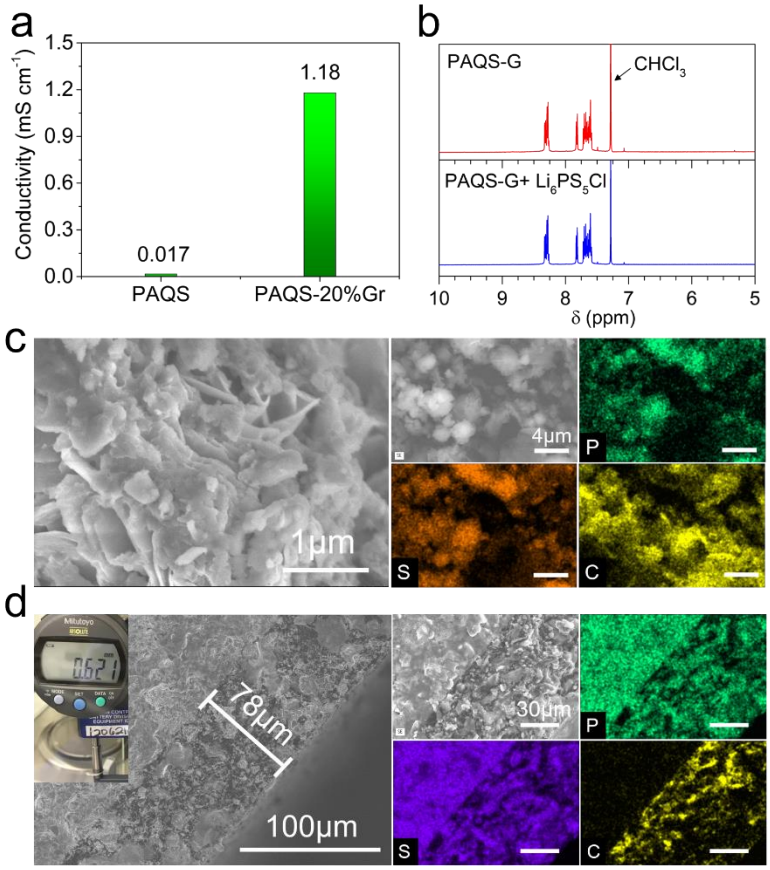

Figure 3. a) Electronic conductivities of pure PAQS polymer and PAQS-20wt.%Gr composite; b) *in-situ* ^{1}H NMR spectra of pristine PAQS-G and PAQS-G+Li_6PS_5Cl mixture (1:1); c) SEM image and EDX mapping of PAQS-G+Li_6PS_5Cl cathode composite; d) cross-section SEM images and EDX mapping of cathode/electrolyte interface.

2.4. Electrochemical performance of PAQS-G cathode in all-solid-state batteries.

The redox behavior of the PAQS-G cathode was investigated by a CV measurement. As shown in Figure 4a, a pair of broad

peaks occur at 1.81 V and 2.08 V, representing the redox behavior of the anthraquinonyl group. The anodic and cathodic peaks were 30 mV more negative compared with the result reported in a liquid electrolyte. The phenomena were possibly ascribed to the impact of different electrolytes on the electron transfer kinetics and the thermodynamic stability of anions.[37] Theoretically, PAQS can undergo a two-electron transfer reaction, corresponding to a capacity of 225 mAh g^{-1}. As shown in Figure 4b, the PAQS-G cathode delivers a reversible capacity of ~178 mAh g^{-1} at 60°C, corresponding to a 79% utilization of the active material. After 200 cycles, the capacity retention was 94% and Coulombic efficiency was nearly 100% despite some fluctuations, which might be caused by the temperature variation of the homemade heating box inside the glovebox. The rate performance was tested from 14 mA g^{-1} (0.07C) to 280 mA g^{-1} (1.5C). As shown in Figure 4c, the PAQS-G cathode maintains 53% of its initial capacity even under 1.5 C, attributed to the efficient electronic percolation network at the electrode level. Galvanostatic intermittent titration technique (GITT) was further employed to study the thermodynamic potential of the electrochemical reaction.[40,41] A series of current pulses (0.05C) were applied, each followed by a relaxation time of 4h. During relaxation, the cell tended to become homogenous by Li^+ diffusion and reached an equilibrium. As shown in Figure 4d, the PAQS-G cathode presents only one voltage plateau after the full relaxation, indicating a one-step solid-solid phase transition between Li_x-PAQS and PAQS. As shown in Figure 4e, polarization curves are obtained from the iR drop during the relaxation, representing the evolution of interfacial resistance under different potentials. The cathode/electrolyte interfacial resistance was the main contributor to the overall cell impedance.[42] During the discharge process, the polarization was relatively small, indicating a stable cathode/electrolyte interface. By contrast, a build-up of polarization was observed at the end of the charge process, indicating that a large Li^+ concentration gradient was established across the cell. This result can be explained by a complete de-association of Li^+ from PAQS backbone and simultaneously, a partial de-lithiation (oxidation) of Li-rich Li_6PS_5Cl electrolyte.[43] Thereby, the evolution of the interfacial resistance during one cycle was potential-dependent. As shown in Figure 4f, similar EIS patterns are displayed at the end of the discharge of the 10th and the 50th cycle, indicating that the evolution of interfacial impedance was very reversible from cycle to cycle, which was beneficial for the cycling stability.

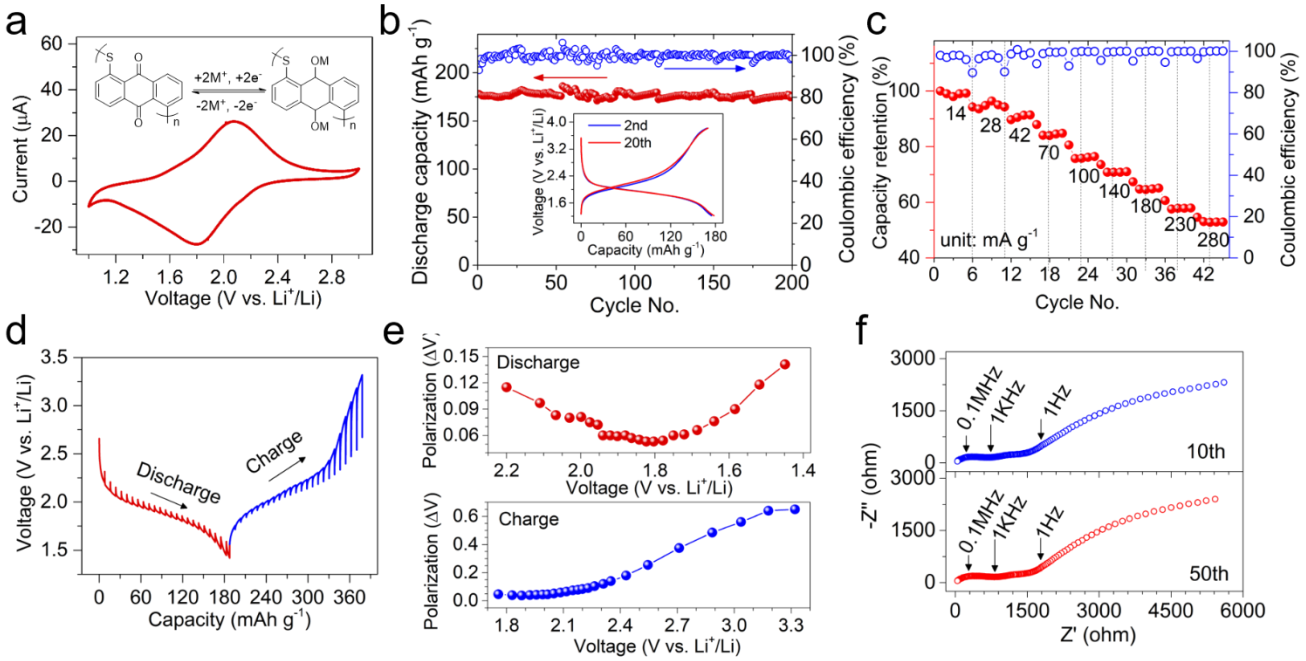

Figure 4. Electrochemical performance of PAQS-G cathode in all-solid-state lithium battery. a) CV profile at a scan rate of 0.05 mV s^{-1}; b) cycling performance at 0.1C (18 mA g^{-1}), inset is the galvanostatic voltage profiles at different cycles; c) rate performance; d) GITT potential profile and e) the corresponding polarization plots during one charge/discharge cycle; f) EIS spectra tested under fully discharged state of different cycles.

Another attractive feature of organic active materials was their ability to be coupled with various metal anodes. Therefore, the Na^+ association/de-association behavior of the PAQS-G cathode was explored in the PAQS-G|Na_3PS_4|$Na_{15}Sn_4$ cell configuration. As shown in Figure 5a, the differential capacity (dQ/dV) curves display a pair of reversible redox peaks located at 1.5 V and 1.7 V vs. Sn/SnNa, respectively. The peaks were consistent with the value achieved from solid-state lithium batteries. The charge/discharge profiles of different cycles are displayed in Figure 5b. The initial cycle differed from the subsequent cycles, possibly caused by a partial irreversible electrolyte degradation to form stable interfaces at the first cycle. As shown in Figure 5c, the PAQS-G cathode displays a capacity retention of 95.5% after 300 cycles at 60°C.

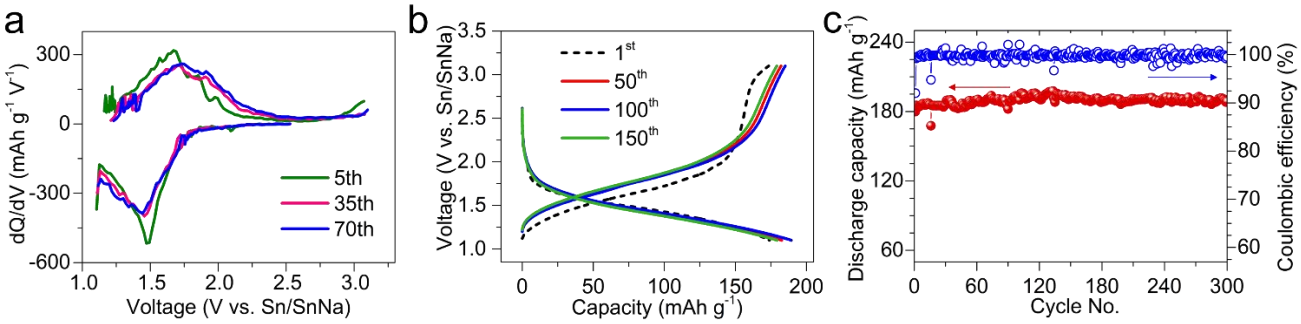

Figure 5. Electrochemical performance of PAQS-G cathode in all-solid-state sodium battery. a) dQ/dV curves at different cycles; b) galvanostatic voltage profiles at different cycles; c) cycling performance at 0.1C (18 mA g^{-1}).

Post-mortem SEM experiment was carried out on the PAQS-G cathode after cycling and the cathode prior to cycling was used as a comparison. Figure 6a displayed the SEM image and EDX mapping of the ball-milled PAQS-G+Na_3PS_4 cathode composite before cycling. The particle size of the cathode composite is around several microns, whose size is consistent with pure Na_3PS_4 particles (Figure S6). However, the cathode composite possesses a much smoother surface morphology compared with Na_3PS_4 particles, implying that the PAQS polymer has been spontaneously wrapped around the glass-ceramic Na_3PS_4 particles during the energy-intensive ball-milling process. Therefore, derived from the elastic nature of polymer material, an intimate interparticle contact can be expected and will facilitate Li^+ transport. EDX mapping presented a uniform distribution of elements, also indicating a well-mixed cathode composite. The cross-section images revealed that the thickness of the cathode layer is 25 μm prior to cycling (Figure 6b) compared to 28 μm after cycling (Figure 6c), implying basically no volume change occurred upon cycling. The corresponding EDX mapping after cycling displayed a uniform distribution of elements within the cathode layer. As shown in Figure 6d, the cycled cathode maintained a dense surface morphology with almost no pores, crack, or voids formation, indicating an intimate interparticle contact within cathode layer throughout cycling. As shown in Figure S7, post-mortem ^1H NMR spectra displayed an almost unchanged chemical structure of PAQS, confirming the high compatibility of PAQS with sulfide electrolyte throughout the electrochemical process.

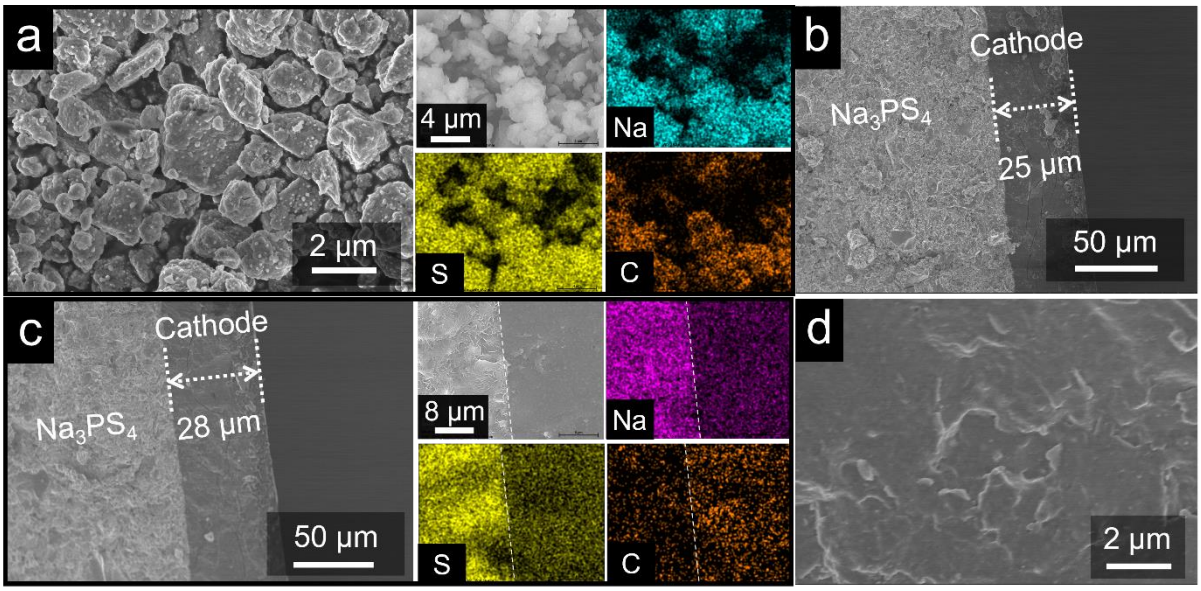

Figure 6. a) SEM image and EDX mapping of the ball-milled PAQS-G+Na_3PS_4 cathode composite after cycling; b) cross-section SEM image of cathode|Na_3PS_4 interface before cycling; c) cross-section SEM image and EDX mapping of cathode|Na_3PS_4 interface after cycling; d) SEM image of cathode surface morphology after cycling.

3. Conclusion

In summary, this work unveiled that small quinone compounds were prone to react with sulfide-based solid electrolytes via a nucleophilic reaction. Poly-(anthraquinonyl sulfide) (PAQS), whose bulky polymer backbone can act as a robust shield against sulfide nucleophile, was proven to be a reliable quinone cathode customized for sulfide-based solid-state batteries. With the incorporation of graphene during the polymerization process, the PAQS-G nanocomposite displayed ameliorated redox kinetics with fast electron transfer. A high utilization of ~79% at active material level and a stable cycling of ≥ 200 cycles were achieved in both solid-state lithium batteries and sodium batteries. We believe the judicious choice protective structures for organic active materials can provide a critical role on mitigating unwanted reaction toward solid electrolytes. The demonstration of the role the steric hindrance effect played on the chemical compatibility offers a guideline for designing organic materials with diversified structure for sustainable and high-performance all-solid-state batteries.

References

[1] J. Janek, W.G. Zeier, A solid future for battery development, Nat. Energy. 1 (2016) 16141.

[2] A. Manthiram, X. Yu, S. Wang, Lithium battery chemistries enabled by solid-state electrolytes, Nat. Rev. Mater. 2 (2017) 1–16.

[3] M.J. Wang, E. Kazyak, N.P. Dasgupta, J. Sakamoto, Transitioning solid-state batteries from lab to market: Linking electro-chemo-mechanics with practical considerations, Joule 5 (2021) 1371–1390.

[4] S. Randau, D.A. Weber, O. Kötz, R. Koerver, P. Braun, A. Weber, E. Ivers-Tiffée, T. Adermann, J. Kulisch, W.G. Zeier, F.H. Richter, J. Janek, Benchmarking the performance of all-solid-state lithium batteries, Nat. Energy. 5 (2020) 259–270.

[5] W. Lee, S. Muhammad, C. Sergey, H. Lee, J. Yoon, Y.-M. Kang, W.-S. Yoon, Advances in the cathode materials for lithium rechargeable batteries, Angew. Chem. Int. Ed. 59 (2020) 2578–2605.

[6] D.H.S. Tan, E.A. Wu, H. Nguyen, Z. Chen, M.A.T. Marple, J.-M. Doux, X. Wang, H. Yang, A. Banerjee, Y.S. Meng, Elucidating reversible electrochemical redox of Li6PS5Cl solid electrolyte, ACS Energy Lett. 4 (2019) 2418–2427.

[7] J. Zhang, C. Zheng, L. Li, Y. Xia, H. Huang, Y. Gan, C. Liang, X. He, X. Tao, W. Zhang, Unraveling the intra and intercycle interfacial evolution of Li_6PS_5Cl-based all-solid-state lithium batteries, Adv. Energy Mater. 10 (2020) 1903311.
[8] J. Auvergniot, A. Cassel, J.-B. Ledeuil, V. Viallet, V. Seznec, R. Dedryvère, Interface stability of argyrodite Li_6PS_5Cl toward $LiCoO_2$, $LiNi_{1/3}Co_{1/3}Mn_{1/3}O_2$, and $LiMn_2O_4$ in bulk all-solid-state batteries, Chem. Mater. 29 (2017) 3883–3890.
[9] G.F. Dewald, S. Ohno, M.A. Kraft, R. Koerver, P. Till, N.M. Vargas-Barbosa, J. Janek, W.G. Zeier, Experimental assessment of the practical oxidative stability of lithium thiophosphate solid electrolytes, Chem. Mater. 31 (2019) 8328–8337.
[10] R. Chen, Q. Li, X. Yu, L. Chen, H. Li, Approaching practically accessible solid-state batteries: Stability issues related to solid electrolytes and interfaces, Chem. Rev. 120 (2020) 6820–6877.
[11] Y. Lu, Q. Zhang, L. Li, Z. Niu, J. Chen, Design strategies toward enhancing the performance of organic electrode materials in metal-ion batteries, Chem. 4 (2018) 2786–2813.
[12] P. Poizot, J. Gaubicher, S. Renault, L. Dubois, Y. Liang, Y. Yao, Opportunities and challenges for organic electrodes in electrochemical energy storage, Chem. Rev. 120 (2020) 6490–6557.
[13] Y. Lu, J. Chen, Prospects of organic electrode materials for practical lithium batteries, Nat. Rev. Chem. 4 (2020) 127–142.
[14] F. Hao, X. Chi, Y. Liang, Y. Zhang, R. Xu, H. Guo, T. Terlier, H. Dong, K. Zhao, J. Lou, Y. Yao, Taming active material-solid electrolyte interfaces with organic cathode for all-solid-state batteries, Joule 3 (2019) 1349–1359.
[15] Y. Kato, S. Hori, T. Saito, K. Suzuki, M. Hirayama, A. Mitsui, M. Yonemura, H. Iba, R. Kanno, High-power all-solid-state batteries using sulfide superionic conductors, Nat. Energy 1 (2016) 16030.
[16] J. Wu, S. Liu, F. Han, X. Yao, C. Wang, Lithium/Sulfide All-Solid-State Batteries using Sulfide Electrolytes, Adv. Mater. 33 (2021) e2000751.
[17] C. Wang, J. Liang, Y. Zhao, M. Zheng, X. Li, X. Sun, All-solid-state lithium batteries enabled by sulfide electrolytes: from fundamental research to practical engineering design, Energy Environ. Sci. 14 (2021) 2577–2619.
[18] Y.-G. Lee, S. Fujiki, C. Jung, N. Suzuki, N. Yashiro, R. Omoda, D.-S. Ko, T. Shiratsuchi, T. Sugimoto, S. Ryu, J.H. Ku, T. Watanabe, Y. Park, Y. Aihara, D. Im, I.T. Han, High-energy long-cycling all-solid-state lithium metal batteries enabled by silver–carbon composite anodes, Nat. Energy 5 (2020) 299–308.
[19] Y. Wu, R. Zeng, J. Nan, D. Shu, Y. Qiu, S.-L. Chou, Quinone electrode materials for rechargeable lithium/sodium ion batteries, Adv. Energy Mater. 7 (2017) 1700278.
[20] Q. Zhao, Z. Zhu, J. Chen, Molecular engineering with organic carbonyl electrode materials for advanced stationary and redox flow rechargeable batteries, Adv. Mater. 29 (2017) 1607007.
[21] T. Yokoji, Y. Kameyama, N. Maruyama, H. Matsubara, High-capacity organic cathode active materials of 2,2′-bis-p-benzoquinone derivatives for rechargeable batteries, J. Mater. Chem. A 4 (2016) 5457–5466.
[22] A. Katritzky, D. Fedoseyenko, P. Mohapatra, P. Steel, Reactions of p-benzoquinone with sulfur nucleophiles, Synthesis 2008 (2008) 777–787.
[23] C. Luo, X. Ji, J. Chen, K.J. Gaskell, X. He, Y. Liang, J. Jiang, C. Wang, Solid-state electrolyte anchored with a carboxylated azo compound for all-solid-state lithium batteries, Angew. Chem. Int. Ed. 57 (2018) 8567–8571.
[24] X. Chi, Y. Liang, F. Hao, Y. Zhang, J. Whiteley, H. Dong, P. Hu, S. Lee, Y. Yao, Tailored organic electrode material compatible with sulfide electrolyte for stable all-solid-state sodium batteries, Angew. Chem. Int. Ed. 57 (2018) 2630–2634.
[25] X. Chi, F. Hao, J. Zhang, X. Wu, Y. Zhang, S. Gheytani, Z. Wen, Y. Yao, A high-energy quinone-based all-solid-state sodium metal battery, Nano Energy 62 (2019) 718–724.
[26] J. Zhang, Z. Chen, Q. Ai, T. Terlier, F. Hao, Y. Liang, H. Guo, J. Lou, Y. Yao, Microstructure engineering of solid-state composite cathode via solvent-assisted processing, Joule (2021). https://doi.org/10.1016/j.joule.2021.05.017.
[27] X. Yang, Y. Hu, N. Dunlap, X. Wang, S. Huang, Z. Su, S. Sharma, Y. Jin, F. Huang, X. Wang, S.-H. Lee, W. Zhang, A truxenone-based covalent organic framework as an all-solid-state lithium-ion battery cathode with high capacity, Angew.

Chem. Int. Ed. 59 (2020) 20385–20389.
[28] H. Huang, T.H. Lambert, Electrophotocatalytic C-H heterofunctionalization of Arenes, Angew. Chem. Int. Ed. 60 (2021) 11163–11167.
[29] H. Huang, T.H. Lambert, Electrophotocatalytic SN Ar reactions of unactivated aryl fluorides at ambient temperature and without base, Angew. Chem. Int. Ed. 59 (2020) 658–662.
[30] W. Ji, H. Huang, X. Zhang, D. Zheng, T. Ding, T.H. Lambert, D. Qu, A redox-active organic salt for safer Na-ion batteries, Nano Energy 72 (2020) 104705.
[31] W. Ji, H. Huang, X. Huang, X. Zhang, D. Zheng, T. Ding, J. Chen, T.H. Lambert, D. Qu, A redox-active organic cation for safer high energy density Li-ion batteries, J. Mater. Chem. A 8 (2020) 17156–17162.
[32] C. Hänsel, P.V. Kumar, D. Kundu, Stack pressure effect in Li_3PS_4 and Na_3PS_4 based alkali metal solid-state cells: The dramatic implication of interlayer growth, Chem. Mater. 32 (2020) 10501–10510.
[33] T. Krauskopf, S.P. Culver, W.G. Zeier, Local tetragonal structure of the cubic superionic conductor Na_3PS_4, Inorg. Chem. 57 (2018) 4739–4744.
[34] J. Lee, M.J. Park, Tattooing dye as a green electrode material for lithium batteries, Adv. Energy Mater. 7 (2017) 1602279.
[35] J. Ruhl, L.M. Riegger, M. Ghidiu, W.G. Zeier, Impact of solvent treatment of the superionic argyrodite Li_6PS_5Cl on solid-state battery performance, Adv. Energy Sustainable Res. 2 (2021) 2000077.
[36] Z. Song, T. Xu, M.L. Gordin, Y.-B. Jiang, I.-T. Bae, Q. Xiao, H. Zhan, J. Liu, D. Wang, Polymer-graphene nanocomposites as ultrafast-charge and -discharge cathodes for rechargeable lithium batteries, Nano Lett. 12 (2012) 2205–2211.
[37] Z. Song, H. Zhan, Y. Zhou, Anthraquinone based polymer as high performance cathode material for rechargeable lithium batteries, Chem. Commun. 4 (2009) 448–450.
[38] S. Burkhardt, M.S. Friedrich, J.K. Eckhardt, A.C. Wagner, N. Bohn, J.R. Binder, L. Chen, M.T. Elm, J. Janek, P.J. Klar, Charge transport in single NCM cathode active material particles for lithium-ion batteries studied under well-defined contact conditions, ACS Energy Lett. 4 (2019) 2117–2123.
[39] X.-Y. Qiu, Q.-C. Zhuang, Q.-Q. Zhang, R. Cao, P.-Z. Ying, Y.-H. Qiang, S.-G. Sun, Electrochemical and electronic properties of $LiCoO_2$ cathode investigated by galvanostatic cycling and EIS, Phys. Chem. Chem. Phys. 14 (2012) 2617–2630.
[40] X. Li, J. Liang, X. Li, C. Wang, J. Luo, R. Li, X. Sun, High-performance all-solid-state Li–Se batteries induced by sulfide electrolytes, Energy Environ. Sci. 11 (2018) 2828–2832.
[41] W. Weppner, R.A. Huggins, Determination of the kinetic parameters of mixed-conducting electrodes and application to the system Li_3Sb, J. Electrochem. Soc. 124 (1977) 1569–1578.
[42] W. Ji, D. Zheng, X. Zhang, T. Ding, D. Qu, A kinetically stable anode interface for Li_3YCl_6-based all-solid-state lithium batteries, J. Mater. Chem. A 9 (2021) 15012–15018.
[43] T.K. Schwietert, V.A. Arszelewska, C. Wang, C. Yu, A. Vasileiadis, N.J.J. de Klerk, J. Hageman, T. Hupfer, I. Kerkamm, Y. Xu, E. van der Maas, E.M. Kelder, S. Ganapathy, M. Wagemaker, Clarifying the relationship between redox activity and electrochemical stability in solid electrolytes, Nat. Mater. 19 (2020) 428–435.